Asphericity can cause Nonuniform Lithium Intercalation in Battery Active Particles

Aashutosh MISTRY,[1,a,*] Thomas HEENAN,[2,3,b] Kandler SMITH,[4,c] Paul SHEARING[2,3,d] and Partha P. MUKHERJEE[5,e]

[1] Chemical Sciences and Engineering Division, Argonne National Laboratory, Lemont, Illinois 60439, United States
[2] Electrochemical Innovation Laboratory, Department of Chemical Engineering, University College London, London WC1E 7JE, United Kingdom
[3] The Faraday Institution, Quad One, Harwell Science and Innovation Campus, Didcot OX11 0RA, United Kingdom
[4] Transportation and Hydrogen Systems Center, National Renewable Energy Laboratory, Golden, Colorado 80401, United States
[5] School of Mechanical Engineering, Purdue University, West Lafayette, Indiana 47907, United States

Abstract

Uniform intercalation is desired to enable next-generation Li-ion batteries. While we expect nonuniformity in materials undergoing a phase change, single-phase intercalation materials such as nickel manganese cobalt oxide are believed to lithiate uniformly at the particle-electrolyte interface. However, recent imaging reveals nonuniform lithiation. Motivated by this discrepancy, we examine if aspherical particle shape can cause such nonuniformity since conventional belief is based on spherical particle theory. We obtain real particle geometries using rapid lab-based X-ray computed tomography and subsequently perform physics-based calculations accounting for electrochemical reactions at the particle/ electrolyte interface and lithium transport inside

the particle bulk. The aspherical geometry breaks the symmetry and causes nonuniform reaction distribution. Such nonuniformity is exacerbated as the particle becomes more aspherical. The proposed mechanism represents a fundamental limit on achievable lithiation uniformity in aspherical particles in the absence of other mechanisms causing inhomogeneity such as grain structure, nonuniform carbon-binder coating, etc.
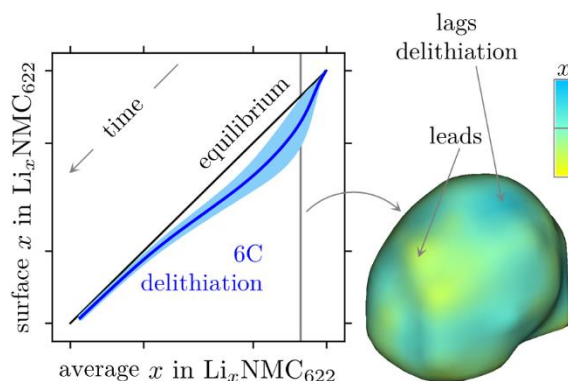
In an intercalation battery such as lithium-ion, energy is fundamentally stored in active material particles[1,2]. Surrounding these active particles, the porous battery electrodes contain additional phases like carbon-binder domain and electrolyte-filled pore network to facilitate finite rate operation[3–10]. In the past decade, the contributions of these additional phases and the corresponding porous structure have been examined[11–33] through various theoretical and experimental techniques. Consequently, new insights have emerged to engineer the porous electrode structures for improved battery operation. In comparison, particle-scale intercalation behavior is believed to be well-understood. Conventionally, we

---

* Corresponding author: amistry@anl.gov
[a] ORCID: 0000 – 0002 – 4359 – 4975
[b] ORCID: 0000 – 0001 – 9912 – 4772
[c] ORCID: 0000 – 0001 – 7011 – 0377
[d] ORCID: 0000 – 0002 – 1387 – 9531
[e] ORCID: 0000 – 0001 – 7900 – 7261

think intercalation leads to concentric concentration distribution[1,34–40] where finite diffusivity is responsible for forming concentration gradients between the particle center and surface. And any departure from such expectations[15,41–48], for example, nonuniform lithiation on the particle surface, is attributed to nonlinear material effects such as multiphase intercalation[38,40,49–53] (refer to **section S1**). Such effects are not expected to occur in single-phase intercalation materials like nickel manganese cobalt oxide where lithiation happens via the solid solution mechanism. However, some recent studies[13,54–59] do reveal nonuniform lithiation on the surface of such active material particles as shown in **Figure 1**(a),(b). The active material particles in these experiments[13,54–59] are not spherical, while the conventional understanding of single-phase intercalation is primarily based on calculations for spherical particles.

Motivated by this disconnect between recent observations and the conventional understanding, we question if the aspherical particle shape can cause the observed inhomogeneity at the particle-electrolyte surface. To systematically answer this question, we obtain NMC_{622} particle geometries using a rapid lab-based X-ray computed tomography method[60] established for high-throughput statistical studies on particle morphologies (relevant details are provided in **section S2**). As shown in **Figure 1**(c), such a particle is not spherical. NMC_{622} is chosen as an exemplar material for multiple reasons. NMC_{622} is one of the low-cobalt lithium intercalation hosts being pursued. Compared to other high-nickel NMC materials, it exhibits a narrower particle size distribution, thus allowing for statistically meaningful particle samples in the imaged volume[60]. Moreover, the material properties (**Figure 1**(d)-(e)) relevant for modeling particle-scale intercalation have been reasonably characterized in the literature[61–64]. As shown in **Figure 1**(d), the open circuit potential for NMC_{622} exhibits a single-phase intercalation behavior since voltage plateaux are absent.

Herein, we model the intercalation behavior of such particles using the lithium conservation equation

$$\frac{\partial c}{\partial t} = \nabla \cdot (\mathbb{D} \nabla c) \tag{1}$$

where c is the local lithium concentration and $\mathbb{D}$ is the corresponding chemical diffusivity (**Figure 1**(f)). The electrochemical reaction at the particle surface is modeled using the Butler-Volmer kinetics

$$i_{\mathrm{app}} = i_0 \left\{ e^{\frac{F(V-U)}{2RT}} - e^{\frac{-F(V-U)}{2RT}} \right\} \tag{2}$$

where i_{app} is the local reaction current density and V is the particle voltage relative to the counter electrode. Eq. [2] includes two material properties: open circuit potential, U (**Figure 1**(d)) and exchange current density, i_0 (**Figure 1**(e)). Eq. [2] serves as a boundary condition for Eq. [1]

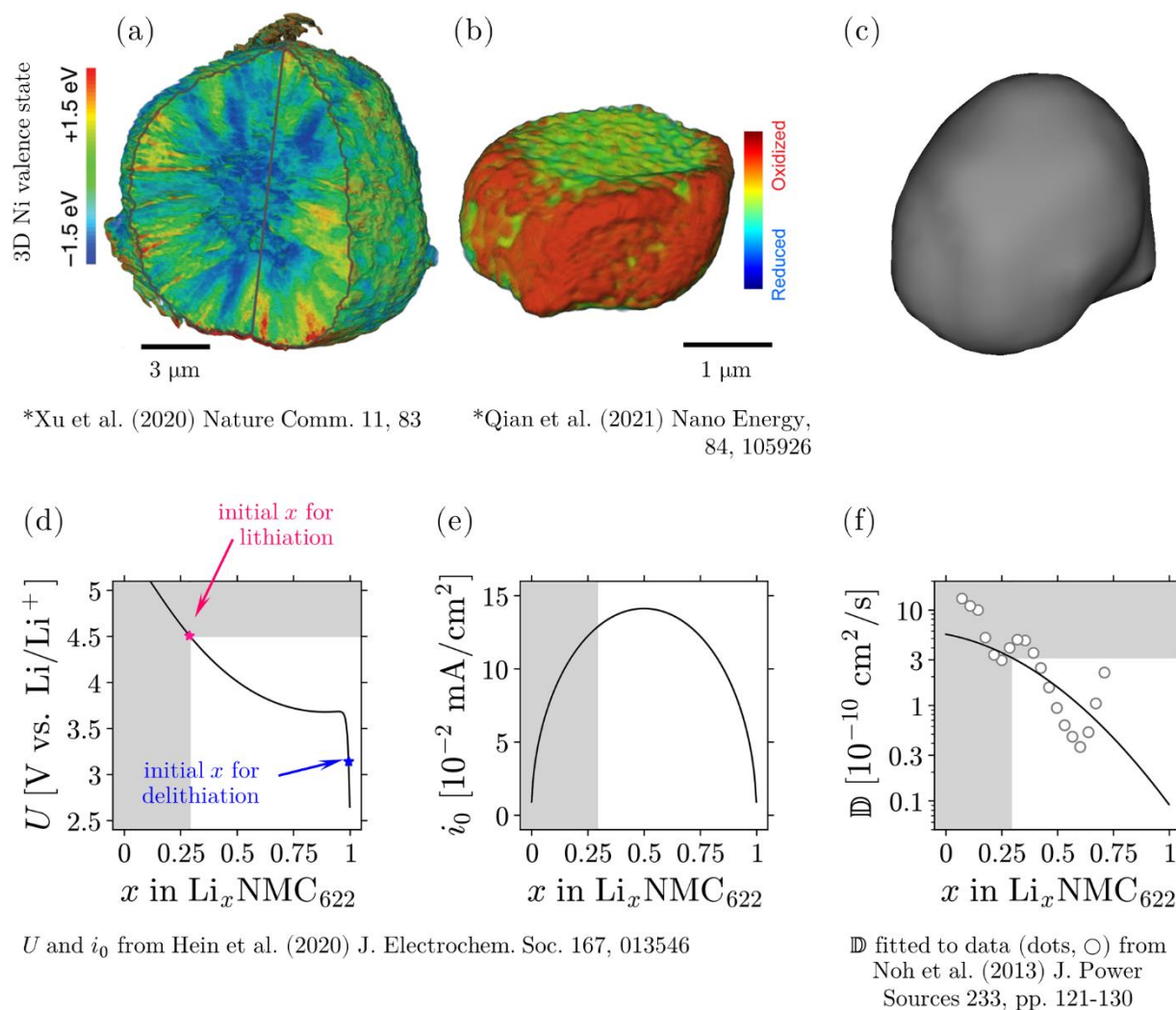$$-\mathbb{D} \nabla c \cdot \hat{n} = \frac{i_{\mathrm{app}}}{F} \tag{3}$$

Figure 1. (a), (b) Examples of imaged inhomogeneity in NMC particles[55,58]. The inhomogeneity in the Ni valence state correlates to the degree of lithiation, x. (c) Representative aspherical particle shape for the present study. The particle geometry is obtained using X-ray computed tomography. (d)-(f) Material properties contributing to particle-scale intercalation behavior and their dependence on degree of lithiation, x, for NMC$_{622}$[61,62]. (d) Open Circuit Potential, U. (e) Exchange current density, i_0. (f) Chemical diffusivity, $\mathbb{D}$, of Li$^+$ in the host material. When these particles are electrochemically intercalated between 2.5 and 4.5V, the corresponding changes in the material property are constrained in the white (unshaded) space of these plots. i_0 in (e) also depends on Li$^+$ concentration in the adjoining electrolyte which is kept constant at 1M.

Since we are interested in understanding the particle-scale effects, the electrolyte and the counter electrode are not explicitly modeled (refer to **section S3** for more details). Such a situation can be experimentally realized by electrochemically operating individual active particles against a lithium electrode[65]. The description so far is identical to the literature[1,8,10,16,36,61,66]. However, unlike these studies, we cannot assume uniform reaction distribution beforehand. Such a distribution of i_{app} is constrained by

$$\bar{\iota}_{\text{app}} = \frac{1}{a}\int_a i_{\text{app}} \, da = \frac{1}{a}\int_a i_0 \left\{ e^{\frac{F(V-U)}{2RT}} - e^{\frac{-F(V-U)}{2RT}} \right\} da \qquad [4]$$

Here, $\bar{\iota}_{\text{app}}$ is average current density on the particle surface and is defined by theoretical capacity, Q, C-rate, and particle surface area, a. The entire particle is at the same voltage, V. Both U and i_0 vary with local lithium content, $x = c/c_{\text{max}}$. If the particle surface is uniformly lithiated, Eq. [4] predicts identical current density at every location (the spherical particle exhibits such, $i_{\text{app}} = \bar{\iota}_{\text{app}}$, behavior), otherwise reaction rates are distributed nonuniformly.
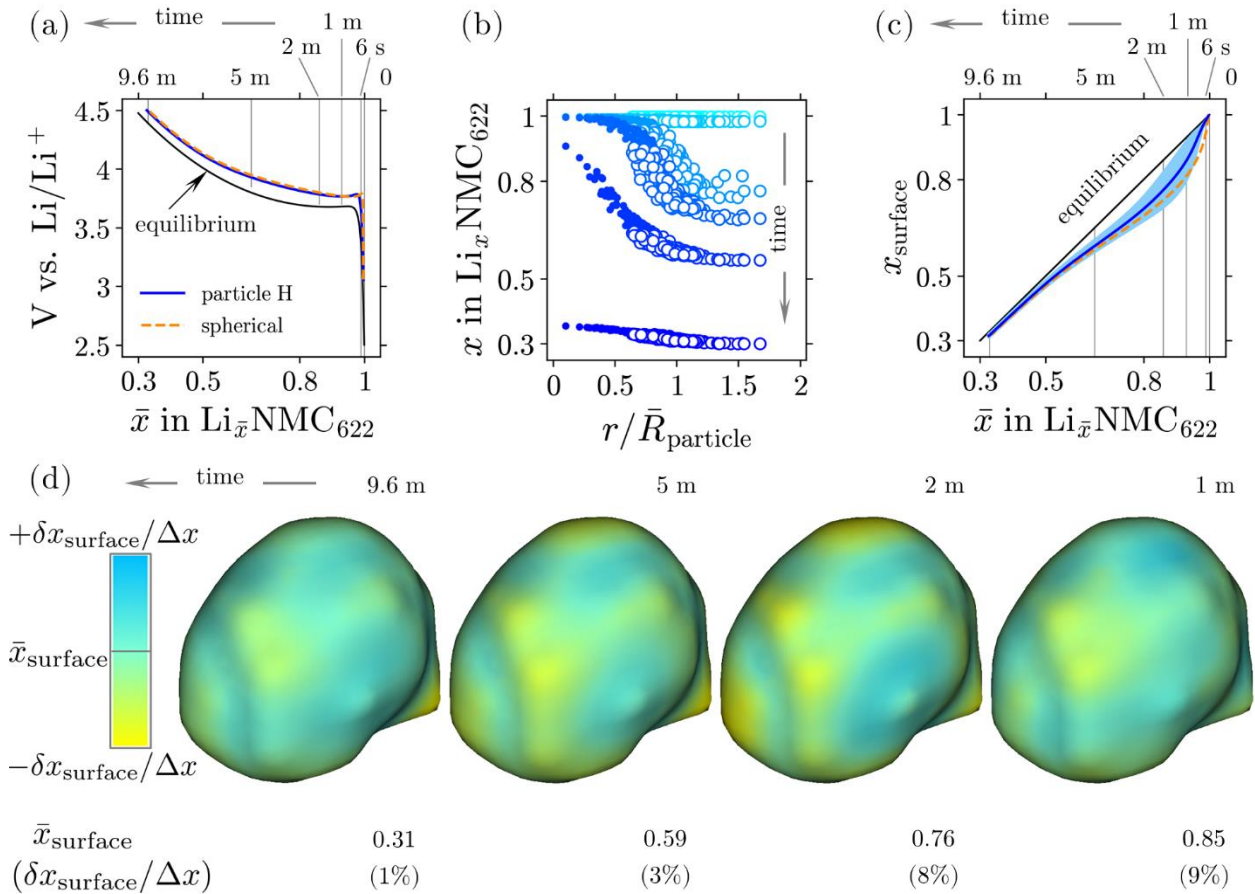

Figure 2. 6C delithiation behavior of the representative particle (**Figure 1**(c)). The volume of the particle is identical to a spherical particle with a 2.5 μm radius. (a) Changes in particle voltage during delithiation. For comparison, the voltage of an equal volume spherical particle delithiated under identical conditions is shown. OCP provides the equilibrium delithiation behavior. (b) Corresponding evolution in local lithiation, x. The filled dots (●) indicate interior locations, and the open dots (○) are material points on particle surface in contact with electrolyte. Different color shades refer to different times. (c) Statistics of delithiation on the particle surface. During infinitely slow (equilibrium) delithiation, every surface point has the same x as the particle averaged degree of lithiation, $\bar{x}$. The solid curve departing from this 45° line shows the average x on the surface of the aspherical particle. The shaded region around this curve identifies the standard deviation, $\delta x_{\text{surface}}$, in x_{surface} at every time instant. For comparison, x_{surface} for a spherical particle is shown using a dashed curve. (d) The distribution of x_{surface} field at representative time instances. The representative time instances for (b) and (d) are

marked on (a) and (c) using incomplete thin vertical lines. Note that $r = 0$ in (b) represents the centroid of the particle. For a spherical particle, all surface points are at $r = \bar{R}_{\text{particle}}$. Thus, (b) also illustrates the spatial distribution of surface points from the centroid.

Figure 2 presents the deintercalation of an aspherical particle at a 6C rate (representative of the futuristic extreme fast charging application[67]). The particle is initially nearly lithiated, $x \approx 0.99$. The results are generated by solving Eqs. [1]-[4] over the particle geometry shown in **Figure 1**(c). As shown in **Figure 2**(a), the particle voltage is higher than U at each particle-averaged intercalation state, $\bar{x}$. For comparison, calculations are also performed on an equal volume spherical particle. For equal volumes, both particles have identical theoretical capacities and experience the same average current density, $\bar{i}_{\text{app}}$. Hence, any difference is related to the aspherical shape. While the difference between the voltage response of these two particles is imperceptible in **Figure 2**(a), the concentration distributions in **Figure 2**(b) are drastically different. For a spherical particle, all surface locations are at distance, $r/\bar{R}_{\text{particle}} = 1$, from the centroid. In contrast, for an aspherical particle, surface points are located at different distances from the centroid. More importantly, not all the surface points (open symbols in **Figure 2**(b)) have identical lithiation. Each color represents lithium distribution at a specific time instance marked in **Figure 2**(a) using thin vertical lines. To further illustrate this surface inhomogeneity, **Figure 2**(c) describes the evolution of surface concentration using two descriptors – average surface concentration, $\bar{x}_{\text{surface}}$ (shown as a solid line) and deviation, $\delta x_{\text{surface}}$ (shown as an error bar around this line). For comparison, the surface concentration of the spherical particle is shown using a dashed curve, and the equilibrium behavior as a 45° line. The difference between the aspherical and spherical particles is more pronounced in terms of concentration profiles (e.g., **Figure 2**(c)) in contrast to voltage evolution in **Figure 2**(a). To visualize this surface inhomogeneity relative to the particle geometry, **Figure 2**(d) superimposes concentration profiles on particle geometry at representative time instances. Specific x values for the color scale in **Figure 2**(d) are different at each time instance and can be mapped to the same color scale using $\bar{x}_{\text{surface}}$ and $\delta x_{\text{surface}}$. The inhomogeneity in surface lithiation, $\delta x_{\text{surface}}$, is as high as ~10% of the lithiation window (note that as per the definition of standard deviation, $\delta x_{\text{surface}} < (x_{\text{surface,max}} - x_{\text{surface,min}})$).

Figure 3 examines the causation for the inhomogeneous lithiation shown in **Figure 2**. At the start of delithiation ($t = 0$ in **Figure 3**), all locations have identical lithium content, and U, i_0 are identical across the surface. In turn, i_{app}, is uniform as shown in **Figure 3**(c). During delithiation, the electrochemical reaction decreases x at the surface, while diffusion from interior locations counter this tendency. Since the surface locations farther from the centroid have longer diffusion lengths, for uniform i_{app} these locations will experience more delithiation and larger $r/\bar{R}_{\text{particle}}$ locations will experience more negative dx/dt in **Figure 3**(d).
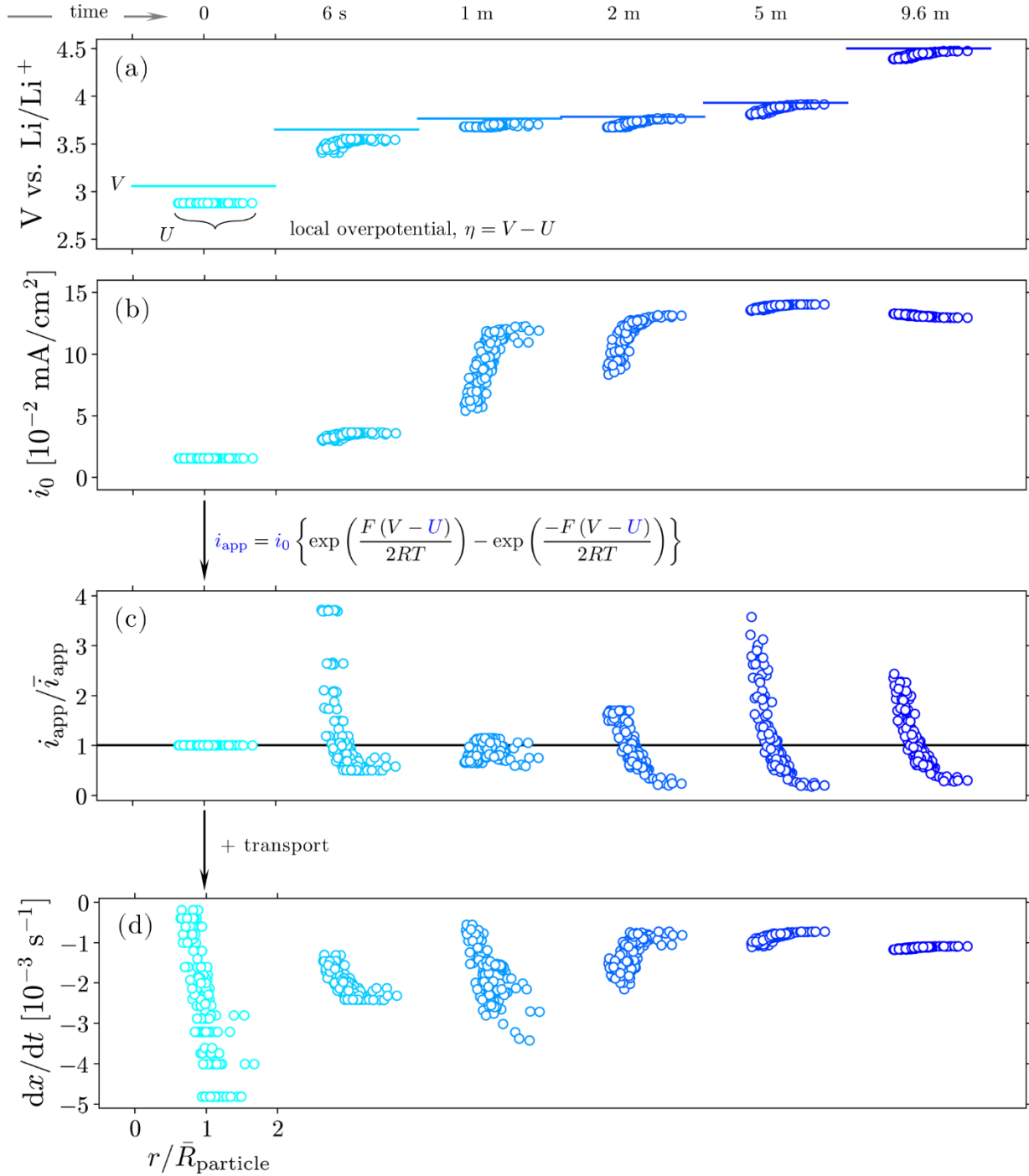
Figure 3. Examining the mechanistic origins of inhomogeneity observed during 6C delithiation of a representative aspherical particle in **Figure 2**. Open symbols (○) are the surface distributions of (a) U (b) i_0 (c) i_{app} and (d) dx/dt. Surface distribution of (a) U and (b) i_0 relates to the variation in $x_{surface}$ shown in **Figure 2**(b) at respective time instances. The particle voltage, V, is such that the particle averaged delithiation rate is 6C. V values corresponding to each time instant are shown in (a) using solid lines. The local distribution of reaction current, i_{app}, in (c) is determined by V and surface distributions in U, i_0. (d) Instantaneous changes in lithiation extent, dx/dt, at surface locations are jointly determined by the reaction distribution (c) and resistance to Li$^+$ transport from the surface locations to the interior. The local transport resistance is predominantly defined by the distance from the centroid, $r/\bar{R}_{particle}$, and chemical diffusivity, $\mathbb{D}$. A more lithiated surface location farther away from the centroid exhibits a higher transport resistance. The color schemes are identical to **Figure 2**(b) and refer to the same time instances.

This imbalance triggers inhomogeneous surface delithiation. As time elapses, a location with a slightly smaller x has a higher U (as per **Figure 1**(d)). During delithiation, the particle voltage, V, is greater than the highest U. Thus, locations lagging delithiation, experience a higher overpotential, $\eta = V - U$, and equivalently a larger local reaction. This distribution is opposite to the diffusion lengths. More lithium deficient locations still lead delithiation but experience a smaller instantaneous change compared to $t = 0$. Fields shown at 6 seconds in **Figure 3** exemplify such a behavior. During these initial moments, the changes in U are more drastic compared to i_0 given the nearly vertical U profile close to $x \approx 1$ in **Figure 1**(d). Instead, at 1 min, changes in U are smaller compared to i_0. Resultant opposite distributions of η (**Figure 3**(a)) and i_0 (**Figure 3**(b)) give rise to nearly uniform reaction distribution in **Figure 3**(c), and the longer diffusion lengths dominate surface delithiation in **Figure 3**(d). Such competitive reaction and diffusion effects amplify inhomogeneity at early times. As time passes by, the variations in U become stronger and in turn, η drives local current distribution. Consequently, the locations lagging delithiation experience a higher local current and the inhomogeneity decreases at late times as seen in **Figure 2**(b),(c).

Thus, the inhomogeneity is triggered by the distribution of diffusion lengths and its growth is related to stronger concentration dependence of material properties close to a fully lithiated state. At later times when the overpotential drives reaction distribution, inhomogeneity decays. **Figure S2** further justifies the role of concentration-dependent material properties in amplifying inhomogeneity. The inhomogeneity is smaller when either i_0 or $\mathbb{D}$ are constant. Even when both i_0 and $\mathbb{D}$ are constant (**Figure S2**(d),(h)), concentration-dependent U, and distribution of diffusion lengths cause inhomogeneity.

Given the coupled effects of concentration-dependent material properties and aspherical geometry, the inhomogeneous lithiation cannot qualify as a reaction- or transport-limited effect (as is typically expected[40]). Instead, the observed inhomogeneity is a joint outcome of reaction and transport interactions. Consequently, either increasing particle size (**Figure S3**) or faster deintercalation (**Figure S4**) leads to greater surface inhomogeneities. Except for **Figure S3**, all other results are for identical particle volumes (chosen to be the volume of a 2.5 μm radius spherical particle).

Note that, some surface locations experience currents as high as four times the average current, i.e., 24C for the 6C operation (**Figure 3**(c)). Such stark inhomogeneity is detrimental and likely causes accelerated mechanical degradation[68,69] compared to a particle experiencing uniform 6C current at every surface location.

The aspherical particle shape also causes inhomogeneities during lithiation (discharging) of this particle as discussed in **Figures S5 – S7**.
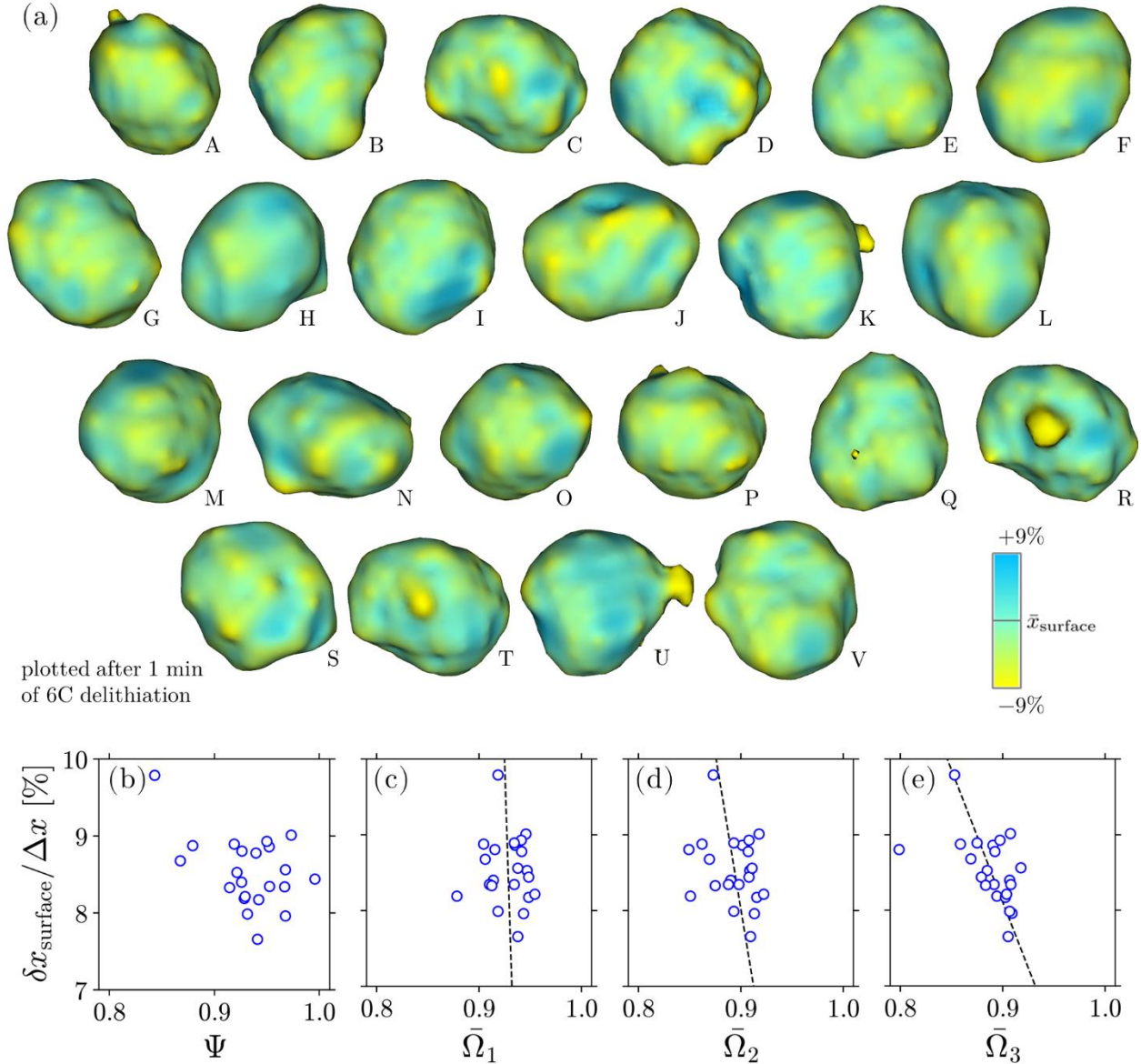
Figure 4. Multiple aspherical particles from **Table S1** are examined to identify universality in the intercalation inhomogeneity. (a) x_{surface} fields for each particle after 1 min of 6C delithiation. Each particle has an identical volume, i.e., theoretical Li storage capacity. Hence the variations in (a) are due to differences in their shapes. (b) Variation in $\delta x_{\mathrm{surface}}/\Delta x$ with sphericity, Ψ. Alternatively, (c)-(e) correlate this inhomogeneity against three moment invariant shape descriptors, $\bar{\Omega}_1, \bar{\Omega}_2, \bar{\Omega}_3$. Linear fits are plotted to assist visualization of the underlying trends. Since Ψ is not a unique identifier of particle shape, the correlation is poor. For a perfect sphere $\bar{\Omega}_1 = \bar{\Omega}_2 = \bar{\Omega}_3 = 1$. As $\bar{\Omega}_3$ decreases from 1, the number of vertices decreases (sphere has infinite vertices; $\bar{\Omega}_3 = 0.405$ for tetrahedron – a 3D shape with the least number of vertices, four). $\bar{\Omega}_1$ and $\bar{\Omega}_2$ represent shape variations for the same basic morphology, for example, sphere and ellipsoid have $\bar{\Omega}_3 = 1$ but the ellipsoid has $\bar{\Omega}_1, \bar{\Omega}_2 < 1$. Inhomogeneity grows as the particle becomes more aspherical in (c)-(e). Note that most of these particles have $\Psi > 0.9$ but behave differently than spherical particles.

To explore the universality of the nonuniform lithium intercalation in an aspherical particle, 6C delithiation is simulated for multiple particles imaged from the same electrode (refer to **Table S1** for geometrical details). **Figure 4**(a) plots surface concentrations for each

of these particles after 1 min of 6C delithiation. Inhomogeneity is observed across all particles. In each instance, the protruded locations, i.e., longer diffusion lengths, are leading delithiation. This is more apparent in particles A, C, J, K, R, S, T, and U. Alternatively, valley locations are lagging delithiation as visible in particles D, J, K, and L. Since these particles have identical volumes, the nonuniform lithiation is related to the aspherical particle shape. Hence, the degree of nonuniformity, $\delta x_{\text{surface}}$ should be correlated to particle shape descriptor(s). While sphericity, Ψ, is easier to compute and often used as a shape descriptor, it is a biased indicator of particle shape. As shown in **Figure 4**(b), even if these particles do not look spherical, $\Psi \gtrsim 0.9$. For example, particle L is distinctly nonspherical but has $\Psi = 0.99$. MacSleyne, Simmons, and DeGraef[70] proposed unbiased shape descriptors, $\overline{\Omega}_1, \overline{\Omega}_2, \overline{\Omega}_3$, based on the moment of inertia tensor. In **Figure 4**(c)-(e), lithiation inhomogeneity is correlated to $\overline{\Omega}_1, \overline{\Omega}_2, \overline{\Omega}_3$. The spherical particle has $\overline{\Omega}_1 = \overline{\Omega}_2 = \overline{\Omega}_3 = 1$. All other shapes have $\overline{\Omega}_1, \overline{\Omega}_2, \overline{\Omega}_3 < 1$ and $\delta x_{\text{surface}}$ appears to increase at smaller $\overline{\Omega}_1, \overline{\Omega}_2, \overline{\Omega}_3$. Dashed lines in **Figure 4**(c)-(e) are sketched to assist visualization. It is interesting to note that all these particles are obtained from the same electrode volume but exhibit an appreciable variation in particle shape.

Thus, aspherical particle shape can break the symmetry in reaction and transport interactions and cause nonuniform intercalation at the particle surface. Such inhomogeneities are observed even for relatively simple single-phase intercalation materials like NMC. While additional effects of grain structure[55], compositional variations[58], nonuniform carbon-binder coating[27,71] or electrode heterogeneities[11,72] cause nonuniform intercalation of active particles, the aspherical particle shape mechanism is active in the absence of other effects and represents a fundamental limit on the achievable lithiation uniformity. It is interesting to note that such nonuniform lithiation takes place without a distinct voltage signature. Hence, porous electrode performance predictions are reasonably accurate with spherical particle assumptions. However, the lithiation nonuniformities become important when the lithiation is imaged, especially under *operando* conditions[15]. Moreover, the associated inhomogeneous current distribution likely causes accelerated degradation. This mechanism is practically relevant for extreme fast charging, batteries for electric flight, and thick electrodes (where active particles close to the separator experience much higher currents[73]), all of which are important for the next-generation intercalation batteries. Since more aspherical particles exhibit increased inhomogeneity, such an effect can be minimized by controlling particle shape during manufacturing.

Supporting Information includes

- Checklist[74] documenting key aspects of the present work
- Nomenclature explaining mathematical symbols used for discussion
- S1. Fundamental Difference between Solid Solution and Phase Transformation Intercalation Behavior (Figure S1)
- S2. X-ray Computed Tomography to Obtain Particle Geometries (Table S1)
- S3. Modeling for Particle-scale Electrochemical Intercalation (Figures S2 – S7)

References

(1) Doyle, M.; Fuller, T. F.; Newman, J. Modeling of Galvanostatic Charge and Discharge of the Lithium/Polymer/Insertion Cell. *J. Electrochem. Soc.* **1993**, *140* (6), 1526–1533. https://doi.org/10.1149/1.2221597.

(2) Newman, J.; Balsara, N. P. *Electrochemical Systems, 4e*; John Wiley & Sons, 2021.

(3) Zheng, H.; Yang, R.; Liu, G.; Song, X.; Battaglia, V. S. Cooperation between Active Material, Polymeric Binder and Conductive Carbon Additive in Lithium Ion Battery Cathode. *J. Phys. Chem. C* **2012**, *116* (7), 4875–4882. https://doi.org/10.1021/jp208428w.

(4) Liu, G.; Zheng, H.; Song, X.; Battaglia, V. S. Particles and Polymer Binder Interaction: A Controlling Factor in Lithium-Ion Electrode Performance. *J. Electrochem. Soc.* **2012**, *159* (3), A214–A221. https://doi.org/10.1149/2.024203jes.

(5) Newman, J.; Tiedemann, W. Porous-electrode Theory with Battery Applications. *AIChE J.* **1975**, *21* (1), 25–41. https://doi.org/10.1002/aic.690210103.

(6) Bae, C. J.; Erdonmez, C. K.; Halloran, J. W.; Chiang, Y. M. Design of Battery Electrodes with Dual-Scale Porosity to Minimize Tortuosity and Maximize Performance. *Adv. Mater.* **2013**, *25* (9), 1254–1258. https://doi.org/10.1002/adma.201204055.

(7) Ebner, M.; Chung, D. W.; García, R. E.; Wood, V. Tortuosity Anisotropy in Lithium-Ion Battery Electrodes. *Adv. Energy Mater.* **2014**, *4* (5). https://doi.org/10.1002/aenm.201301278.

(8) Mistry, A. N.; Smith, K.; Mukherjee, P. P. Secondary-Phase Stochastics in Lithium-Ion Battery Electrodes. *ACS Appl. Mater. Interfaces* **2018**, *10* (7), 6317–6326. https://doi.org/10.1021/acsami.7b17771.

(9) Zielke, L.; Hutzenlaub, T.; Wheeler, D. R.; Manke, I.; Arlt, T.; Paust, N.; Zengerle, R.; Thiele, S. A Combination of X-Ray Tomography and Carbon Binder Modeling: Reconstructing the Three Phases of LiCoO2 Li-Ion Battery Cathodes. *Adv. Energy Mater.* **2014**, *4* (8). https://doi.org/10.1002/aenm.201301617.

(10) Ji, Y.; Zhang, Y.; Wang, C.-Y. Li-Ion Cell Operation at Low Temperatures. *J. Electrochem. Soc.* **2013**, *160* (4), A636–A649. https://doi.org/10.1149/2.047304jes.

(11) Mistry, A. N.; Usseglio-Viretta, F. L. E.; Colclasure, A. M.; Smith, K.; Mukherjee, P. P. Fingerprinting Redox Heterogeneity in Electrodes during Extreme Fast Charging. *J. Electrochem. Soc.* **2020**, *167* (9), 090542. https://doi.org/10.1149/1945-7111/ab8fd7.

(12)   Mistry, A.; Trask, S.; Dunlop, A.; Jeka, G.; Polzin, B.; Mukherjee, P. P.; Srinivasan, V. Quantifying Negative Effects of Carbon-Binder Networks from Electrochemical Performance of Porous Li-Ion Electrodes. *J. Electrochem. Soc.* **2021**, *168* (7), 70536. https://doi.org/10.1149/1945-7111/ac1033.

(13)   Tian, C.; Xu, Y.; Nordlund, D.; Lin, F.; Liu, J.; Sun, Z.; Liu, Y.; Doeff, M. Charge Heterogeneity and Surface Chemistry in Polycrystalline Cathode Materials. *Joule* **2018**, *2* (3), 464–477. https://doi.org/https://doi.org/10.1016/j.joule.2017.12.008.

(14)   Yu, Y.-S.; Farmand, M.; Kim, C.; Liu, Y.; Grey, C. P.; Strobridge, F. C.; Tyliszczak, T.; Celestre, R.; Denes, P.; Joseph, J.; et al. Three-Dimensional Localization of Nanoscale Battery Reactions Using Soft X-Ray Tomography. *Nat. Commun.* **2018**, *9* (1), 921. https://doi.org/10.1038/s41467-018-03401-x.

(15)   Merryweather, A. J.; Schnedermann, C.; Jacquet, Q.; Grey, C. P.; Rao, A. Operando Optical Tracking of Single-Particle Ion Dynamics in Batteries. *Nature* **2021**, *594* (7864), 522–528. https://doi.org/10.1038/s41586-021-03584-2.

(16)   Higa, K.; Wu, S.-L.; Parkinson, D. Y.; Fu, Y.; Ferreira, S.; Battaglia, V.; Srinivasan, V. Comparing Macroscale and Microscale Simulations of Porous Battery Electrodes. *J. Electrochem. Soc.* **2017**, *164* (11), E3473–E3488. https://doi.org/10.1149/2.0501711jes.

(17)   Goldin, G. M.; Colclasure, A. M.; Wiedemann, A. H.; Kee, R. J. Three-Dimensional Particle-Resolved Models of Li-Ion Batteries to Assist the Evaluation of Empirical Parameters in One-Dimensional Models. *Electrochim. Acta* **2012**, *64*, 118–129. https://doi.org/10.1016/j.electacta.2011.12.119.

(18)   Mistry, A. N.; Smith, K.; Mukherjee, P. P. Electrochemistry Coupled Mesoscale Complexations in Electrodes Lead to Thermo-Electrochemical Extremes. *ACS Appl. Mater. Interfaces* **2018**, *10* (34), 28644–28655. https://doi.org/10.1021/acsami.8b08993.

(19)   Yao, K. P. C.; Okasinski, J. S.; Kalaga, K.; Shkrob, I. A.; Abraham, D. P. Quantifying Lithium Concentration Gradients in the Graphite Electrode of Li-Ion Cells Using: Operando Energy Dispersive X-Ray Diffraction. *Energy Environ. Sci.* **2019**, *12* (2), 656–665. https://doi.org/10.1039/c8ee02373e.

(20)   Lu, X.; Bertei, A.; Finegan, D. P.; Tan, C.; Daemi, S. R.; Weaving, J. S.; O'Regan, K. B.; Heenan, T. M. M.; Hinds, G.; Kendrick, E.; Brett, D. J. L.; Shearing, P. R. 3D Microstructure Design of Lithium-Ion Battery Electrodes Assisted by X-Ray Nano-Computed Tomography and Modelling. *Nat. Commun.* **2020**, *11* (1), 2079. https://doi.org/10.1038/s41467-020-15811-x.

(21)   Holtz, M. E.; Yu, Y.; Gunceler, D.; Gao, J.; Sundararaman, R.; Schwarz, K. A.; Arias, T. A.; Abruña, H. D.; Muller, D. A. Nanoscale Imaging of Lithium Ion Distribution During In Situ Operation of Battery Electrode and Electrolyte. *Nano Lett.* **2014**, *14* (3), 1453–1459. https://doi.org/10.1021/nl404577c.

(22)   Harris, S. J.; Lu, P. Effects of Inhomogeneities--Nanoscale to Mesoscale--on the Durability of Li-Ion Batteries. *J. Phys. Chem. C* **2013**, *117*, 6481–6492.

(23)   Forouzan, M. M.; Mazzeo, B. A.; Wheeler, D. R. Modeling the Effects of Electrode Microstructural Heterogeneities on Li-Ion Battery Performance and Lifetime. *J. Electrochem. Soc.* **2018**, *165* (10), A2127–A2144. https://doi.org/10.1149/2.1281809jes.

(24)   Charalambous, H.; Borkiewicz, O. J.; Colclasure, A. M.; Yang, Z.; Dunlop, A. R.; Trask, S. E.; Jansen, A. N.; Bloom, I. D.; Ruett, U.; Wiaderek, K. M.; Ren, Y. Comprehensive Insights into Nucleation, Autocatalytic Growth, and Stripping Efficiency for Lithium Plating in Full Cells. *ACS Energy Lett.* **2021**, *6* (10), 3725–3733. https://doi.org/10.1021/acsenergylett.1c01640.

(25)   Ho, A. S.; Parkinson, D. Y.; Finegan, D. P.; Trask, S. E.; Jansen, A. N.; Tong, W.; Balsara, N. P. 3D Detection of Lithiation and Lithium Plating in Graphite Anodes during Fast Charging. *ACS Nano* **2021**, *15* (6), 10480–10487. https://doi.org/10.1021/acsnano.1c02942.

(26)   Okasinski, J. S.; Shkrob, I. A.; Rodrigues, M.-T. F.; Raj, A.; Prado, A. Y. R.; Chuang, A. C.; Pidaparthy, S. S.; Abraham, D. P. Time-Resolved X-Ray Operando Observations of Lithiation Gradients across the Cathode Matrix and Individual Oxide Particles during Fast Cycling of a Li-Ion Cell. *J. Electrochem. Soc.* **2021**, *168* (11), 110555. https://doi.org/10.1149/1945-7111/ac3941.

(27)   Ferraro, M. E.; Trembacki, B. L.; Brunini, V. E.; Noble, D. R.; Roberts, S. A. Electrode Mesoscale as a Collection of Particles: Coupled Electrochemical and Mechanical Analysis of NMC Cathodes. *J. Electrochem. Soc.* **2020**, *167* (1), 013543. https://doi.org/10.1149/1945-7111/ab632b.

(28)   Chouchane, M.; Rucci, A.; Lombardo, T.; Ngandjong, A. C.; Franco, A. A. Lithium Ion Battery Electrodes Predicted from Manufacturing Simulations: Assessing the Impact of the Carbon-Binder Spatial Location on the Electrochemical Performance. *J. Power Sources* **2019**, *444*. https://doi.org/10.1016/j.jpowsour.2019.227285.

(29)   Yang, Y.; Xu, R.; Zhang, K.; Lee, S.; Mu, L.; Liu, P.; Waters, C. K.; Spence, S.; Xu, Z.; Wei, C.; et al. Quantification of Heterogeneous Degradation in Li-Ion Batteries. *Adv. Energy Mater.* **2019**, *9* (25), 1900674. https://doi.org/10.1002/aenm.201900674.

(30)   Santos, D. A.; Andrews, J. L.; Bai, Y.; Stein, P.; Luo, Y.; Zhang, Y.; Pharr, M.; Xu, B.-X.; Banerjee, S. Bending Good Beats Breaking Bad: Phase Separation Patterns in Individual Cathode Particles upon Lithiation and Delithiation. *Mater. Horizons* **2020**, *7* (12), 3275–3290. https://doi.org/10.1039/D0MH01240H.

(31) Andrews, J. L.; Stein, P.; Santos, D. A.; Chalker, C. J.; De Jesus, L. R.; Davidson, R. D.; Gross, M. A.; Pharr, M.; Batteas, J. D.; Xu, B.-X.; Banerjee, S. Curvature-Induced Modification of Mechano-Electrochemical Coupling and Nucleation Kinetics in a Cathode Material. *Matter* **2020**, *3* (5), 1754–1773. https://doi.org/https://doi.org/10.1016/j.matt.2020.08.030.

(32) Luo, Y.; Bai, Y.; Mistry, A.; Zhang, Y.; Zhao, D.; Sarkar, S.; Handy, J. V; Rezaei, S.; Chuang, A. C.; Carrillo, L.; Wiaderek, K.; Pharr, M.; Xie, K.; Mukherjee, P. P.; Xu, B.-X.; Banerjee, S. Effect of Crystallite Geometries on Electrochemical Performance of Porous Intercalation Electrodes by Multiscale Operando Investigation. *Nat. Mater.* **2021**, 1–11. https://doi.org/10.1038/s41563-021-01151-8.

(33) Park, J.; Zhao, H.; Kang, S. D.; Lim, K.; Chen, C.-C.; Yu, Y.-S.; Braatz, R. D.; Shapiro, D. A.; Hong, J.; Toney, M. F.; Bazant, M. Z.; Chueh, W. C. Fictitious Phase Separation in Li Layered Oxides Driven by Electro-Autocatalysis. *Nat. Mater.* **2021**, *20* (7), 991–999. https://doi.org/10.1038/s41563-021-00936-1.

(34) Christensen, J.; Newman, J. A Mathematical Model of Stress Generation and Fracture in Lithium Manganese Oxide. *J. Electrochem. Soc.* **2006**, *153* (6), A1019. https://doi.org/10.1149/1.2185287.

(35) Zhang, X.; Shyy, W.; Marie Sastry, A. Numerical Simulation of Intercalation-Induced Stress in Li-Ion Battery Electrode Particles. *J. Electrochem. Soc.* **2007**, *154* (10), A910. https://doi.org/10.1149/1.2759840.

(36) Santhanagopalan, S.; Guo, Q.; Ramadass, P.; White, R. E. Review of Models for Predicting the Cycling Performance of Lithium Ion Batteries. *J. Power Sources* **2006**, *156* (2), 620–628. https://doi.org/10.1016/j.jpowsour.2005.05.070.

(37) Dees, D. W.; Kawauchi, S.; Abraham, D. P.; Prakash, J. Analysis of the Galvanostatic Intermittent Titration Technique (GITT) as Applied to a Lithium-Ion Porous Electrode. *J. Power Sources* **2009**, *189* (1), 263–268. https://doi.org/https://doi.org/10.1016/j.jpowsour.2008.09.045.

(38) Dees, D. W.; Rodrigues, M.-T. F.; Kalaga, K.; Trask, S. E.; Shkrob, I. A.; Abraham, D. P.; Jansen, A. N. Apparent Increasing Lithium Diffusion Coefficient with Applied Current in Graphite. *J. Electrochem. Soc.* **2020**, *167* (12), 120528. https://doi.org/10.1149/1945-7111/abaf9f.

(39) Srinivasan, V.; Newman, J. Discharge Model for the Lithium Iron-Phosphate Electrode. *J. Electrochem. Soc.* **2004**, *151* (10), A1517. https://doi.org/10.1149/1.1785012.

(40) Fraggedakis, D.; Nadkarni, N.; Gao, T.; Zhou, T.; Zhang, Y.; Han, Y.; Stephens, R. M.; Shao-Horn, Y.; Bazant, M. Z. A Scaling Law to Determine Phase Morphologies during Ion Intercalation. *Energy Environ. Sci.* **2020**, *13* (7), 2142–2152. https://doi.org/10.1039/D0EE00653J.

(41) Jongwoo, L.; Yiyang, L.; Hein, A. D.; Hongyun, S.; Chul, L. S.; Peng, B.; A., C. D.; Xuzhao, L.; Norman, J.; Young-sang, Y.; J., S. N.; A., S. D.; Z., B. M.; Tolek, T.; C., C. W. Origin and Hysteresis of Lithium Compositional Spatiodynamics within Battery Primary Particles. *Science (80-.).* **2016**, *353* (6299), 566–571. https://doi.org/10.1126/science.aaf4914.

(42) Xu, Y.; Hu, E.; Zhang, K.; Wang, X.; Borzenets, V.; Sun, Z.; Pianetta, P.; Yu, X.; Liu, Y.; Yang, X.-Q.; Li, H. In Situ Visualization of State-of-Charge Heterogeneity within a LiCoO2 Particle That Evolves upon Cycling at Different Rates. *ACS Energy Lett.* **2017**, *2* (5), 1240–1245. https://doi.org/10.1021/acsenergylett.7b00263.

(43) Kuppan, S.; Xu, Y.; Liu, Y.; Chen, G. Phase Transformation Mechanism in Lithium Manganese Nickel Oxide Revealed by Single-Crystal Hard X-Ray Microscopy. *Nat. Commun.* **2017**, *8* (1), 14309. https://doi.org/10.1038/ncomms14309.

(44) Yoo, H. D.; Jokisaari, J. R.; Yu, Y.-S. S.; Kwon, B. J.; Hu, L.; Kim, S.; Han, S.-D. D.; Lopez, M.; Lapidus, S. H.; Nolis, G. M.; Ingram, B. J.; Bolotin, I. L.; Ahmed, S.; Klie, R. F.; Vaughey, J. T.; Fister, T. T.; Cabana, J. Intercalation of Magnesium into a Layered Vanadium Oxide with High Capacity. *ACS Energy Lett.* **2019**, *4* (7), 1528–1534. https://doi.org/10.1021/acsenergylett.9b00788.

(45) Xu, Z.; Hou, D.; Kautz, D. J.; Liu, W.; Xu, R.; Xiao, X.; Lin, F. Charging Reactions Promoted by Geometrically Necessary Dislocations in Battery Materials Revealed by In Situ Single-Particle Synchrotron Measurements. *Adv. Mater.* **2020**, *32* (37), 2003417. https://doi.org/https://doi.org/10.1002/adma.202003417.

(46) Gao, T.; Han, Y.; Fraggedakis, D.; Das, S.; Zhou, T.; Yeh, C.-N.; Xu, S.; Chueh, W. C.; Li, J.; Bazant, M. Z. Interplay of Lithium Intercalation and Plating on a Single Graphite Particle. *Joule* **2021**, *5* (2), 393–414. https://doi.org/https://doi.org/10.1016/j.joule.2020.12.020.

(47) De Jesus, L. R.; Horrocks, G. A.; Liang, Y.; Parija, A.; Jaye, C.; Wangoh, L.; Wang, J.; Fischer, D. A.; Piper, L. F. J.; Prendergast, D.; Banerjee, S. Mapping Polaronic States and Lithiation Gradients in Individual V2O5 Nanowires. *Nat. Commun.* **2016**, *7*. https://doi.org/10.1038/ncomms12022.

(48) Zhang, Y.; Yang, Z.; Tian, C. Probing and Quantifying Cathode Charge Heterogeneity in Li Ion Batteries. *J. Mater. Chem. A* **2019**, *7* (41), 23628–23661. https://doi.org/10.1039/C9TA06977A.

(49) Cogswell, D. A.; Bazant, M. Z. Theory of Coherent Nucleation in Phase-Separating Nanoparticles. *Nano Lett.* **2013**, *13* (7), 3036–3041. https://doi.org/10.1021/nl400497t.

(50) Xiang, K.; Yang, K.; Carter, W. C.; Tang, M.; Chiang, Y.-M. Mesoscopic Phase Transition Kinetics in Secondary Particles of Electrode-Active Materials in Lithium-Ion Batteries. *Chem. Mater.* **2018**, *30* (13), 4216–4225. https://doi.org/10.1021/acs.chemmater.7b05407.

(51) Gallagher, K. G.; Dees, D. W.; Jansen, A. N.; Abraham, D. P.; Kang, S.-H. A Volume Averaged Approach to the

Numerical Modeling of Phase-Transition Intercalation Electrodes Presented for Li x C 6 . *J. Electrochem. Soc.* **2012**, *159* (12), A2029–A2037. https://doi.org/10.1149/2.015301jes.

(52) Wang, F.; Tang, M. Thermodynamic Origin of Reaction Non-Uniformity in Battery Porous Electrodes and Its Mitigation. *J. Electrochem. Soc.* **2020**, *167* (12), 120543. https://doi.org/10.1149/1945-7111/abb383.

(53) Harris, S. J.; Rahani, E. K.; Shenoy, V. B. Direct In Situ Observation and Numerical Simulations of Non-Shrinking-Core Behavior in an MCMB Graphite Composite Electrode. *J. Electrochem. Soc.* **2012**, *159* (9), A1501–A1507. https://doi.org/10.1149/2.055209jes.

(54) Mu, L.; Yuan, Q.; Tian, C.; Wei, C.; Zhang, K.; Liu, J.; Pianetta, P.; Doeff, M. M.; Liu, Y.; Lin, F. Propagation Topography of Redox Phase Transformations in Heterogeneous Layered Oxide Cathode Materials. *Nat. Commun.* **2018**, *9* (1), 2810. https://doi.org/10.1038/s41467-018-05172-x.

(55) Xu, Z.; Jiang, Z.; Kuai, C.; Xu, R.; Qin, C.; Zhang, Y.; Rahman, M. M.; Wei, C.; Nordlund, D.; Sun, C.-J.; Xiao, X.; Du, X.-W.; Zhao, K.; Yan, P.; Liu, Y.; Lin, F. Charge Distribution Guided by Grain Crystallographic Orientations in Polycrystalline Battery Materials. *Nat. Commun.* **2020**, *11* (1), 83. https://doi.org/10.1038/s41467-019-13884-x.

(56) Tan, C.; Leach, A. S.; Heenan, T. M. M.; Parks, H.; Jervis, R.; Weker, J. N.; Brett, D. J. L.; Shearing, P. R. Nanoscale State-of-Charge Heterogeneities within Polycrystalline Nickel-Rich Layered Oxide Cathode Materials. *Cell Reports Phys. Sci.* **2021**, 100647. https://doi.org/https://doi.org/10.1016/j.xcrp.2021.100647.

(57) Wang, L.; Liu, T.; Dai, A.; De Andrade, V.; Ren, Y.; Xu, W.; Lee, S.; Zhang, Q.; Gu, L.; Wang, S.; Wu, T.; Jin, H.; Lu, J. Reaction Inhomogeneity Coupling with Metal Rearrangement Triggers Electrochemical Degradation in Lithium-Rich Layered Cathode. *Nat. Commun.* **2021**, *12* (1), 5370. https://doi.org/10.1038/s41467-021-25686-1.

(58) Qian, G.; Huang, H.; Hou, F.; Wang, W.; Wang, Y.; Lin, J.; Lee, S.-J.; Yan, H.; Chu, Y. S.; Pianetta, P.; Huang, X.; Ma, Z.-F.; Li, L.; Liu, Y. Selective Dopant Segregation Modulates Mesoscale Reaction Kinetics in Layered Transition Metal Oxide. *Nano Energy* **2021**, *84*, 105926. https://doi.org/https://doi.org/10.1016/j.nanoen.2021.105926.

(59) Gent, W. E.; Li, Y.; Ahn, S.; Lim, J.; Liu, Y.; Wise, A. M.; Gopal, C. B.; Mueller, D. N.; Davis, R.; Weker, J. N.; Park, J.-H.; Doo, S.-K.; Chueh, W. C. Persistent State-of-Charge Heterogeneity in Relaxed, Partially Charged Li1−xNi1/3Co1/3Mn1/3O2 Secondary Particles. *Adv. Mater.* **2016**, *28* (31), 6631–6638. https://doi.org/https://doi.org/10.1002/adma.201601273.

(60) Heenan, T. M. M.; Llewellyn, A. V; Leach, A. S.; Kok, M. D. R.; Tan, C.; Jervis, R.; Brett, D. J. L.; Shearing, P. R. Resolving Li-Ion Battery Electrode Particles Using Rapid Lab-Based X-Ray Nano-Computed Tomography for High-Throughput Quantification. *Adv. Sci.* **2020**, *7* (12), 2000362. https://doi.org/https://doi.org/10.1002/advs.202000362.

(61) Hein, S.; Danner, T.; Westhoff, D.; Prifling, B.; Scurtu, R.; Kremer, L.; Hoffmann, A.; Hilger, A.; Osenberg, M.; Manke, I.; Wohlfahrt-Mehrens, M.; Schmidt, V.; Latz, A. Influence of Conductive Additives and Binder on the Impedance of Lithium-Ion Battery Electrodes: Effect of Morphology. *J. Electrochem. Soc.* **2020**, *167* (1), 013546. https://doi.org/10.1149/1945-7111/ab6b1d.

(62) Noh, H.-J.; Youn, S.; Yoon, C. S.; Sun, Y.-K. Comparison of the Structural and Electrochemical Properties of Layered Li[NixCoyMnz]O2 (x = 1/3, 0.5, 0.6, 0.7, 0.8 and 0.85) Cathode Material for Lithium-Ion Batteries. *J. Power Sources* **2013**, *233*, 121–130. https://doi.org/https://doi.org/10.1016/j.jpowsour.2013.01.063.

(63) Neumann, A.; Randau, S.; Becker-Steinberger, K.; Danner, T.; Hein, S.; Ning, Z.; Marrow, J.; Richter, F. H.; Janek, J.; Latz, A. Analysis of Interfacial Effects in All-Solid-State Batteries with Thiophosphate Solid Electrolytes. *ACS Appl. Mater. Interfaces* **2020**, *12* (8), 9277–9291. https://doi.org/10.1021/acsami.9b21404.

(64) Cui, S.; Wei, Y.; Liu, T.; Deng, W.; Hu, Z.; Su, Y.; Li, H.; Li, M.; Guo, H.; Duan, Y.; Wang, W.; Rao, M.; Zheng, J.; Wang, X.; Pan, F. Optimized Temperature Effect of Li-Ion Diffusion with Layer Distance in Li(NixMnyCoz)O2 Cathode Materials for High Performance Li-Ion Battery. *Adv. Energy Mater.* **2016**, *6* (4), 1501309. https://doi.org/https://doi.org/10.1002/aenm.201501309.

(65) Tsai, P. C.; Wen, B.; Wolfman, M.; Choe, M. J.; Pan, M. S.; Su, L.; Thornton, K.; Cabana, J.; Chiang, Y. M. Single-Particle Measurements of Electrochemical Kinetics in NMC and NCA Cathodes for Li-Ion Batteries. *Energy Environ. Sci.* **2018**, *11* (4), 860–871. https://doi.org/10.1039/c8ee00001h.

(66) Wu, S.-L.; Zhang, W.; Song, X.; Shukla, A. K.; Liu, G.; Battaglia, V.; Srinivasan, V. High Rate Capability of Li(Ni 1/3 Mn 1/3 Co 1/3)O 2 Electrode for Li-Ion Batteries . *J. Electrochem. Soc.* **2012**, *159* (4), A438–A444. https://doi.org/10.1149/2.062204jes.

(67) Ahmed, S.; Bloom, I.; Jansen, A. N.; Tanim, T.; Dufek, E. J.; Pesaran, A.; Burnham, A.; Carlson, R. B.; Dias, F.; Hardy, K.; et al. Enabling Fast Charging – A Battery Technology Gap Assessment. *J. Power Sources* **2017**, *367*, 250–262. https://doi.org/10.1016/j.jpowsour.2017.06.055.

(68) Allen, J. M.; Weddle, P. J.; Verma, A.; Mallarapu, A.; Usseglio-Viretta, F.; Finegan, D. P.; Colclasure, A. M.; Mai, W.; Schmidt, V.; Furat, O.; Diercks, D.; Tanim, T.; Smith, K. Quantifying the Influence of Charge Rate and Cathode-Particle Architectures on Degradation of Li-Ion Cells through 3D Continuum-Level Damage Models. *J. Power Sources* **2021**, *512*, 230415. https://doi.org/https://doi.org/10.1016/j.jpowsour.2021.230415.

(69) Lin, F.; Zhao, K.; Liu, Y. Heterogeneous Reaction Activities and Statistical Characteristics of Particle Cracking in Battery Electrodes. *ACS Energy Lett.* **2021**, *6* (11), 4065–4070. https://doi.org/10.1021/acsenergylett.1c02135.

(70) MacSleyne, J. P.; Simmons, J. P.; De Graef, M. On the Use of Moment Invariants for the Automated Analysis of 3D Particle Shapes. *Model. Simul. Mater. Sci. Eng.* **2008**, *16* (4). https://doi.org/10.1088/0965-0393/16/4/045008.

(71) Jaiser, S.; Kumberg, J.; Klaver, J.; Urai, J. L.; Schabel, W.; Schmatz, J.; Scharfer, P. Microstructure Formation of Lithium-Ion Battery Electrodes during Drying – An Ex-Situ Study Using Cryogenic Broad Ion Beam Slope-Cutting and Scanning Electron Microscopy (Cryo-BIB-SEM). *J. Power Sources* **2017**, *345*, 97–107. https://doi.org/10.1016/j.jpowsour.2017.01.117.

(72) Mistry, A.; Smith, K.; Mukherjee, P. P. Stochasticity at Scales Leads to Lithium Intercalation Cascade. *ACS Appl. Mater. Interfaces* **2020**, *12* (14), 16359–16366. https://doi.org/10.1021/acsami.9b23155.

(73) Gao, H.; Wu, Q.; Hu, Y.; Zheng, J. P.; Amine, K.; Chen, Z. Revealing the Rate-Limiting Li-Ion Diffusion Pathway in Ultrathick Electrodes for Li-Ion Batteries. *J. Phys. Chem. Lett.* **2018**, *9* (17), 5100–5104. https://doi.org/10.1021/acs.jpclett.8b02229.

(74) Mistry, A.; Verma, A.; Sripad, S.; Ciez, R.; Sulzer, V.; Brosa Planella, F.; Timms, R.; Zhang, Y.; Kurchin, R.; Dechent, P.; et al. A Minimal Information Set To Enable Verifiable Theoretical Battery Research. *ACS Energy Lett.* **2021**, *6* (11), 3831–3835. https://doi.org/10.1021/acsenergylett.1c01710.